Molecular structural mechanics model for the mechanical properties of microtubules

ARTICLE *in* BIOMECHANICS AND MODELING IN MECHANOBIOLOGY · MARCH 2014

Impact Factor: 3.15 · DOI: 10.1007/s10237-014-0564-x · Source: PubMed

2 AUTHORS:

Jin Zhang
Chinese Academy of Sciences
155 PUBLICATIONS **3,052** CITATIONS
SEE PROFILE

C.Y Wang
Swansea University
70 PUBLICATIONS **1,292** CITATIONS
SEE PROFILE

Biomech Model Mechanobiol (2014) 13:1175–1184
DOI 10.1007/s10237-014-0564-x

ORIGINAL PAPER

Molecular structural mechanics model for the mechanical properties of microtubules

Jin Zhang · Chengyuan Wang

Received: 26 October 2013 / Accepted: 20 February 2014 / Published online: 9 March 2014

Abstract The aim of this paper was to develop a structural mechanics (SM) model for the microtubules (MTs) in cells. The technique enables one to study the configuration effect on the mechanical properties of MTs and enjoys greatly improved computational efficiency as compared with molecular dynamics simulations. The SM model shows that the Young's modulus has nearly a constant value around 0.83 GPa, whereas the shear modulus, two orders of magnitude lower, varies considerably with the protofilament number N and helix-start number S. The dependence of the bending stiffness and persistence length on the MT length and protofilament number N is also examined and explained based on the continuum mechanics theories. Specifically, the SM model is found to be in good agreement with available simulation and experiment results, showing its robustness in studying the static deformation of MTs and the potential for characterizing the buckling and vibration of MTs as well as the mechanical behaviour of intermediate and actin filaments.

Keywords Microtubules · Mechanical properties · Configuration effects · Molecular mechanics · Structural mechanics model

Electronic supplementary material The online version of this article (doi:10.1007/s10237-014-0564-x) contains supplementary material, which is available to authorized users.

J. Zhang · C. Wang (✉)
College of Engineering, Swansea University, Singleton Park, Swansea, Wales SA2 8PP, UK
e-mail: chengyuan.wang@swansea.ac.uk

J. Zhang
e-mail: zjdyd1986@163.com

1 Introduction

Microtubules (MTs) are long cylindrically shaped protein filaments that serve as an important structural element of living cells (Alberts et al. 2002; Howard 2001). They are composed of α- and β-tubulin heterodimers, which attach longitudinally with each other in a head-to-tail fashion and bind laterally with a conversed stagger (Alberts et al. 2002; Hawkins et al. 2010; Howard and Hyman 2003). Due to the unique molecular structures, MTs exhibit strong ability to withstand various external loadings and, thus, are responsible for maintaining the cell structural stiffness, functioning as a track for motor proteins to transport organelles and facilitating cell division. The mechanical properties of MTs thus become a current topic of great interest in the areas of cell mechanics and nano-biomaterials.

The first reliable experimental characterization on the mechanical properties of MTs was performed by Mizushima-Sugano et al. (1983) and then was followed by many others based on advanced techniques (Hawkins et al. 2010), such as thermal fluctuations (Gittes et al. 1993; Pampaloni et al. 2006), optical tweezers (Felgner et al. 1996), atomic force microscopy (de Pablo et al. 2003) and hydrodynamic flow (Venier et al. 1994). The Young's modulus and bending stiffness measured for MTs, however, are up to two orders of magnitude different. The possible reasons for such large, method-dependent discrepancy have been reviewed in (Kikumoto et al. 2006). Simultaneously, analytical or computational modelling approaches have also been applied to quantify the mechanical properties of MTs, which include the stochastic models of assembly dynamics (Van Buren et al. 2002), mechanochemical models (VanBuren et al. 2005), the molecular dynamics (MD) simulations (Mitra and Sept 2008; Wu et al. 2012; Gebremichael et al. 2008; Deriu et al. 2007; Sept and MacKintosh 2010), the anisotropic elastic network

models (AENM) (Deriu et al. 2010), the finite elements method (Schaap et al. 2007; Kasas et al. 2004; Donhauser et al. 2010; Mehrbod and Mofrad 2011) and the continuum mechanics models (Sirenko et al. 1996; Wang et al. 2006a, b, 2009; Wang and Zhang 2008; Li 2008). The efforts made so far have significantly expanded the knowledge of the mechanical properties of MTs and advanced the physics behind these unique features.

It is well known that the relationship between molecular structures and mechanical properties is one of the major concerns in the study of advanced nanomaterials. The issue, however, has not yet been discussed in details for MTs consisting of a large number of α and β monomers. This is due to the large uncertainty in the nano-experiments and the formidability in the computation of atomistic simulations (Hawkins et al. 2010; Kikumoto et al. 2006; Pampaloni and Florin 2008). On the other hand, a structural mechanics (SM) model was developed for carbon nanotubes (CNTs), the carbon counterparts of MTs, which accounts for the molecular structures of CNTs like MD simulation but enjoys the much higher computational efficiency (Li and Chou 2003). Such an SM model thus offers an alternative strategy to address the above-mentioned fundamental issue for MTs.

In this paper, the SM model is developed for the first time to construct MTs of different configurations (or molecular structures). The model is then used to quantify the Young's modulus, shear modulus, bending stiffness and persistence length of MTs and examine their dependence on the configuration of MTs, characterized by protofilament (PF) number, helix-start number and the skew angle of MTs. In addition, the SM model is compared with available MD simulations, AENM and experiments to demonstrate its reliability and accuracy in studying the mechanics of MTs.

2 Molecular structures of MTs

In this section, we shall first review the molecular structures of MTs illustrated in Fig. 1. The building blocks of MTs are α- and β-tubulin monomers (Fig. 1a) whose head-to-tail binding constructs a beam-like PF (Fig. 1b). A number of parallel PFs can be aligned to form a PF hollow cylinder, i.e., an MT (Fig. 1c), via the lateral interaction between adjacent PFs. As shown in Fig. 1c, the two adjacent PFs slide relative to each other in the axial direction by a small separation δx. Neighbouring PFs are shifted relatively to each other longitudinally, which results in a (left-handed) helical order in the lateral direction. This unique feature is measured by the helix-start number S which is the longitudinal displacement (in units of monomer size) achieved in one full lateral turn. Thus, MTs are usually represented by the notation of N_S, where N is the number of PFs. In particular, it is observed in vivo and in vitro that N and S of MTs vary widely from 8 to 17

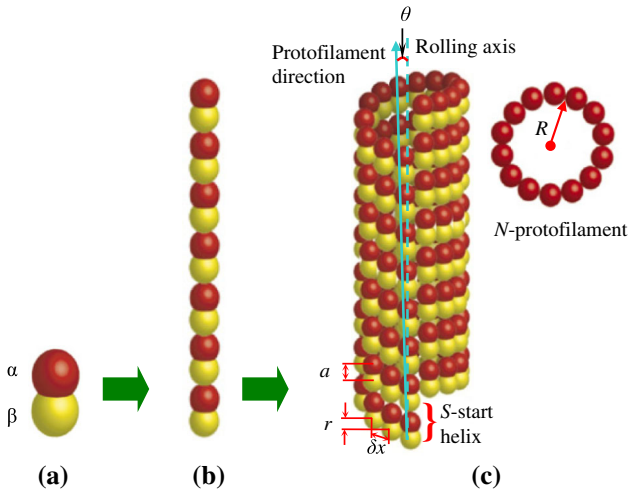

Fig. 1 Representation of (**a**) an $\alpha\beta$-tubulin dimmer, (**b**) a PF and (**c**) an MT structure

and 2 to 4 (Hunyadi et al. 2007), respectively. Accordingly, to retain the favourable lateral interactions between tubulins, the PFs of an MT generally are not parallel with its axis but skew relative to it with a skew angle θ whose value is determined by N and S of the MT (Fig. 1c). It is reported that θ changes from $-2.34°$ of 14_2 to $1.81°$ of 15_4 and that of 13_3 is equal to zero (Chretien and Fuller 2000). The relations among the major factors that determine the molecular structures and geometric size of an MT are as follows (Chretien and Fuller 2000; Hunyadi et al. 2005)

$$r = \frac{Sa}{N} - \delta x \tan(\theta) \tag{1}$$

$$R = \frac{Sa\tan(\theta) + N\delta x}{2\pi} \tag{2}$$

where r is the subunit rise (Fig. 1c), a is the subunit repeat and R is the effective tube radius. As we mentioned above, various MT configurations are observed with different PF number N and helix-start number S. In the present study, we shall focus our attention on the ten MTs of the most common configurations. The vules of N, S, the lattice parameters δx, a, θ and the percentage p (Chretien and Fuller 2000) of ten different MT samples are summarized in Table 1.

3 Structural mechanics model for MTs

The MD simulations can accurately describe the all-atom force fields and interactions between atoms/molecules. It thus is considered as a standard technique for the detailed studies of biomaterials. However, to date, the application of standard MD simulations is limited to relatively small protein complexes (typically comprising $\sim 10^5$ atoms) that is much smaller than real MT fragments (comprising $\sim 10^6$ atoms). A promising strategy to overcome this limitation is to reduce

Table 1 The percentage and lattice parameters of different MT types (Chretien and Fuller 2000)

N_S	*p* (%)	δx (nm)	*a* (nm)	θ (°)
12_2	0.226	5.18	4.05	−1.02
12_3	3.169	5.27	4.04	0.85
13_2	0.033	5.02	4.07	−1.64
13_3	83.661	5.13	4.05	0.00
14_2	0.008	5.08	4.06	−2.34
14_3	11.647	5.16	4.05	−0.68
14_4	0.759	5.05	4.05	0.87
15_3	0.263	5.07	4.05	−1.33
15_4	0.110	5.06	4.04	1.81
16_4	0.035	5.19	4.04	1.17

the number of degrees of freedom by grouping atoms into pseudoatoms (or particles) referred to as beads. This idea serves as the basis of the so-called coarse-grained approach (Chu and Voth 2005). The technique is able to partially overcome the length-scale limitations but still restricted by the inherent time scale (10^{-9}–10^{-6}s) of MD simulations. As a result, further effort is demanded to develop a modelling technique that enables one to analyse the mechanical response of relative large biomaterials like MTs without any limitation on the size and time. To achieve this goal, an SM model is selected as an alternative method. As will be shown later, in this model, the bonds between the tubulin monomers of MTs are considered as the continuum beams whose equivalent material properties can be extracted from MD simulations. The MTs can then be transformed into a frame structures at the nanoscale. Compared with the MD simulations, the present approach possesses following two advantages. First, it can be used for simulating both static and dynamic loadings (Li and Chou 2003). Second, it does not consider thermal vibration of the atoms and treats only "long time" phenomena. The economy in computational cost has been achieved through such simplification. As a result, the technique can enjoy the greatly improved computational efficiency as compared with MD simulations. In the meantime, it still retains the ability to account for the effect of the molecular structures on the mechanical responses of biomaterials. Such an SM model has been used successfully in studying the mechanics of other nanoscale tubules, such as CNTs, a carbon counterpart of MTs (Li and Chou 2003). Very recently, our group has further extended the model to the buckling analysis of boron nitride nanotubes (Zhang et al. 2013). On the other hand, it is worth mentioning that the static SM models do not consider the thermal vibration of individual atoms and are unable to account for the formation and breakage of the chemical bonds between adjacent atoms or proteins. As a result, the present SM model is not applicable for the simulation of the thermal fluctuations of MTs.

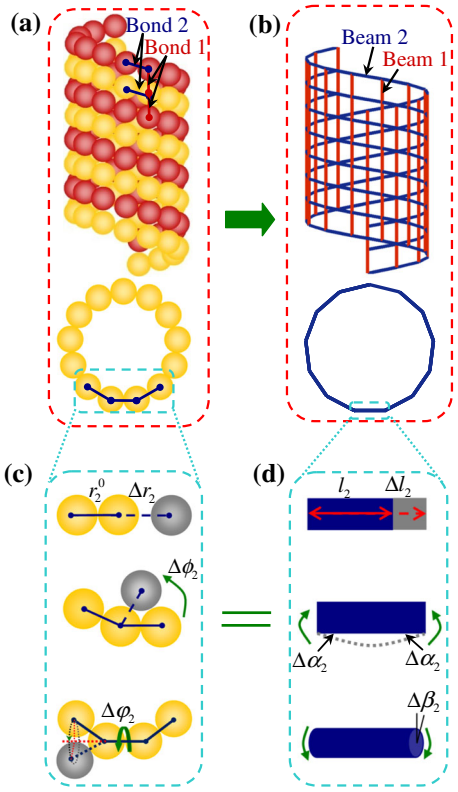

Fig. 2 **a** A molecular representation and **b** a space-frame structure representation of an MT. Potential energies given by the molecular mechanics and structural mechanics are illustrated in (**c**) and (**d**), respectively, where the *yellow* or *blue* colour denotes the initial positions and the *gray* colour shows the positions after deformation

As shown in Fig. 2a, in an MT, there exist two types of interactions between the constitutive monomers. The first one is the longitudinal interaction between α and β monomers in one PF, i.e., the $\alpha\beta$ bond (labelled as bond 1 (the red lines) in Fig. 2a) that forms individual PFs of an MT. The other is the lateral interaction between two α monomers (or two β monomers) in adjacent PFs, i.e., the $\alpha\alpha$ or $\beta\beta$ bond (labelled as bond 2 (the blue lines) in Fig. 2a) that binds the adjacent PFs to construct the cylindrical lateral surface of an MT. Here, it is noted that the mechanical properties of the lateral $\alpha\alpha$ and $\beta\beta$ bonds are quite close. For example, the equivalent stiffness constants measured for the two bonds by MD simulations are around 3 nN/nm (Enemark et al. 2008). Thus, in developing the SM model for an MT, the longitudinal $\alpha\beta$ bond is modelled as elastic beam 1, and the lateral $\alpha\alpha$ and $\beta\beta$ bonds are modelled as elastic beam 2. The molecular structure of an MT can then be considered as a frame structure (Fig. 2b) consisting of beams 1 (the read lines) in the longitudinal direction and beams 2 (the blue lines) in the helical direction.

Based on the molecular mechanics theory, the total steric potential energy stored in an MT (Fig. 2a) can be calculated as a sum of potential energies due to covalent bond inter-

actions provided that the electrostatic interaction and other nonbonded interactions are negligible:

$$U = \sum_{i=1,2} \left(\sum U_i^r + \sum U_i^\phi + \sum U_i^\tau \right) \tag{3}$$

where U_i^r is the bond stretching energy, U_i^ϕ is the angle bending energy and U_i^τ is the dihedral angle torsional potential energy. The subscript 1 denotes $\alpha\beta$ bond interactions, and 2 denotes $\alpha\alpha$ and $\beta\beta$ bond interactions. The deformation pattern associated with U_i^r, U_i^ϕ and U_i^τ, respectively, is illustrated in Fig. 2c for bond 2 (i.e., $\alpha\alpha$ or $\beta\beta$ bonds) on the cross-section of an MT, i.e., the bond stretching (compression) measured by bond length change Δr_i (the initial length is r_i^0), the bond bending due to the in-plane bond angle change $\Delta\phi_i$ (in the plane of two adjacent bonds), and the bond torsion originating from out-of-plane angle change $\Delta\varphi_i$ (out of the plane of three adjacent bonds). Such deformation will also occur for bond 1 (i.e., $\alpha\beta$ bonds) on the lateral surface of an MT. As far as a small deformation is concerned, the harmonic approximation is adequate for describing the potential energy. In this case, U_i^r, U_i^ϕ and U_i^τ in Eq. 3 can be expressed by

$$U_i^r = \frac{1}{2} k_i^r (\Delta r_i)^2, \quad U_i^\phi = \frac{1}{2} k_i^\phi (\Delta\phi_i)^2,$$
$$U_i^\tau = \frac{1}{2} k_i^\tau (\Delta\varphi_i)^2 \quad (i = 1, 2) \tag{4}$$

where k_i^r, k_i^ϕ and k_i^τ are the force constants for bond stretching, bond angle bending and bond torsion, respectively. According to the coarse-grained MD simulations on MTs (Ji and Feng 2011a), the values of these constants are $k_1^r = 3\,\text{nN/nm}$, $k_1^\phi = 2\,\text{nN nm/rad}^2$, $k_1^\tau = 0.04\,\text{nN nm/rad}^2$ for bond 1 (i.e., $\alpha\beta$ interactions) and $k_2^r = 14\,\text{nN/nm}$, $k_2^\phi = 8.5\,\text{nN nm/rad}^2$, $k_2^\tau = 0.17\,\text{nN nm/rad}^2$ for bond 2 (i.e., $\alpha\alpha$ and $\beta\beta$ interactions). These parameter values have been proven to be accurate through a series of MD simulations on the equilibrium conformations of sheet-ended MTs and the structure evolution of MTs during radial indentation (Ji and Feng 2011a, b). Further validation of these values will be conducted later in this study.

On the other hand, in the present SM model of an MT (Fig. 2b), the aforementioned stretching, bending and torsion of the monomer bonds (Fig. 2c) can be modelled by the tension, bending and torsion of the corresponding beams (Fig. 2d) that construct the frame structure shown in Fig. 2b. The theory of structural mechanics indicates that in a frame structure, the deformation of a constitutive beam is entirely controlled by three stiffness parameters, such as the extensional stiffness $Y_i A_i$, the flexural stiffness $Y_i I_i$ and the torsional stiffness $S_i J_i$. Here, Y_i, S_i, A_i, I_i and J_i are, respectively, the Young's modulus, shear modulus, cross-sectional area, moment of inertia and polar inertia of the equivalent beam. The total potential energy in the frame structure of an MT then reads

$$U = \sum_{i=1,2} \left(\sum U_i^A + \sum U_i^M + \sum U_i^T \right) \tag{5}$$

where U_i^A, U_i^M and U_i^T are the strain energies of a beam due to tension, bending and torsion, respectively. The subscript 1 and 2 denote the strain energies of beam 1 and 2. Again, under the assumption of small deformation, the strain energies can be expressed by

$$U_i^A = \frac{1}{2} \frac{Y_i A_i}{l_i} (\Delta l_i)^2, \quad U_i^M = \frac{1}{2} \frac{Y_i I_i}{l_i} (2\Delta\alpha_i)^2,$$
$$U_i^T = \frac{1}{2} \frac{S_i J_i}{l_i} (\Delta\beta_i)^2 \quad (i = 1, 2) \tag{6}$$

where l_i, Δl_i, $\Delta\alpha_i$ and $\Delta\beta_i$, respectively, are the initial length, length change, bending angle and twisting angle of the beams (Fig. 2d).

To characterize the mechanical behaviour of an MT by using the present SM model, it is required that before any external loading is applied $l_1 = r_1^0 = a$ in the longitudinal direction and $l_2 = r_2^0 = \sqrt{r^2 + \delta x^2}$ in the helical direction (Fig. 1c). On the other hand, once external loading is applied, the following geometric relations hold true between an MT and its SM model (see Fig. 2c,d)

$$\Delta l_i = \Delta r_i, \quad 2\Delta\alpha_i = \Delta\phi_i, \quad \Delta\beta_i = \Delta\varphi_i \quad (i = 1, 2) \tag{7}$$

In particular, the local potential energy U_i^r, U_i^ϕ and U_i^τ (Eq. 4) of an MT should be equal to U_i^A, U_i^M and U_i^T (Eq. 6) of its SM model. This energy equivalency combined with Eqs. (4), (6) and (7) leads to the following equations that can be used to determine the values of $Y_i A_i$, $Y_i I_i$ and $S_i J_i$ for the SM model.

$$\frac{Y_i A_i}{l_i} = k_i^r, \quad \frac{Y_i I_i}{l_i} = k_i^\phi, \quad \frac{S_i J_i}{l_i} = k_i^\tau \quad (i = 1, 2) \tag{8}$$

With the known values of $Y_i A_i$, $Y_i I_i$ and $S_i J_i$, one can obtain the nodal displacements of the equivalent frame structures of MTs following the standard solution procedure of the stiffness matrix method as detailed in the Supplementary Materials or Weaver and Gere (1990).

4 Young's modulus and shear modulus of MTs

In this section, the present SM model was employed to measure the Young's modulus and shear modulus of MTs, and examine their dependence on the configuration of MTs. The free-fixed end conditions (i.e., one end is free and the other is fixed) were considered for the sample MTs unless otherwise

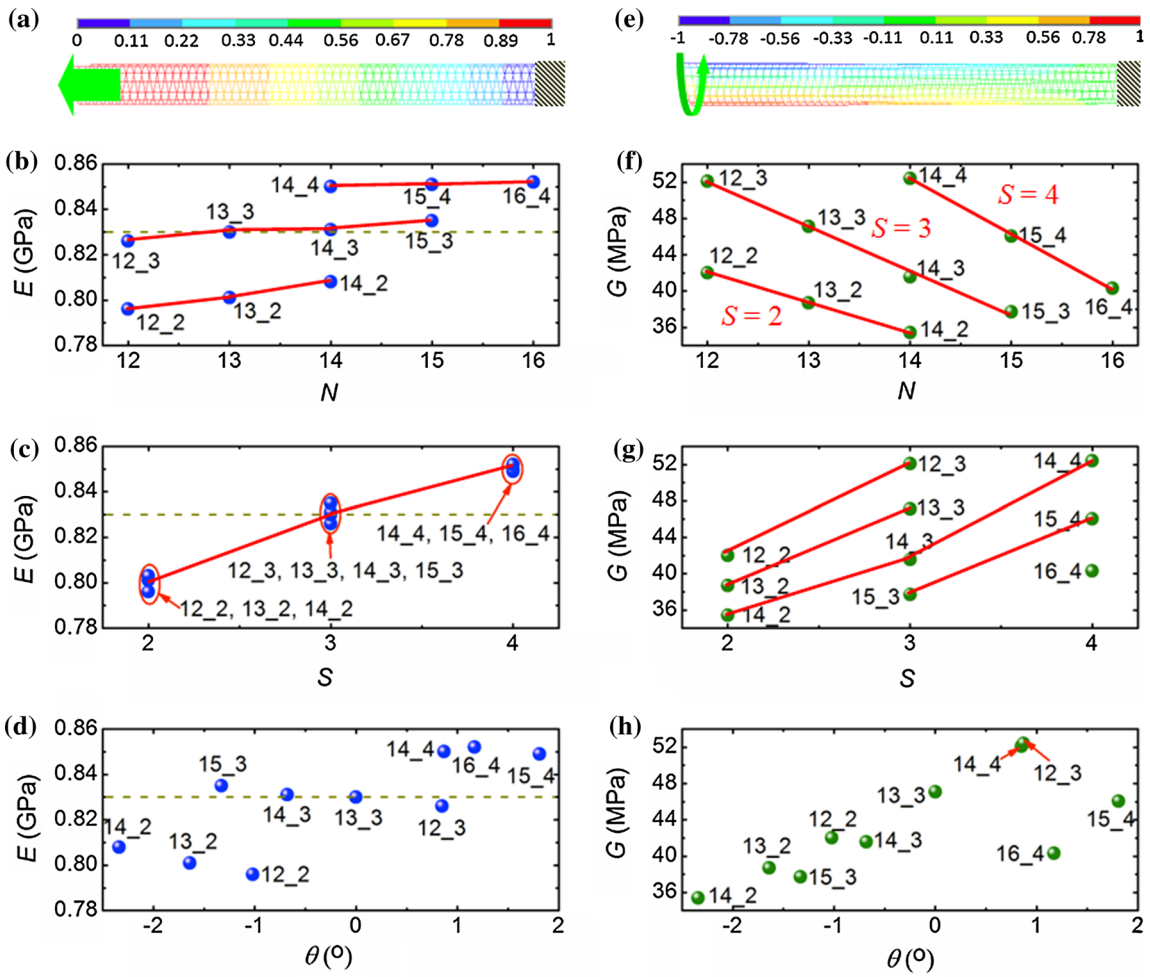

Fig. 3 **a** The deformation of an MT under a tension and the Young's modulus E as a function of (**b**) the PF number N, (**c**) the helix-start number S and (**d**) the PF skew angle θ; (**e**) The deformation of an MT under a torsion and the shear modulus G as a function of (**f**) N, (**g**) S and (**h**) θ

specified. The details of the ten sample MTs were summarized in Table 1.

4.1 Configuration effect on Young's modulus

First, we measured the Young's modulus of the sample MTs in tensile test, where the free end of the MTs was subject to an axial force (Fig. 3a). The Young's modulus E was then evaluated via $E = \frac{F_1/A_0}{\Delta L/L_0}$, in which F_1 is the applied force, $A_0 = 2\pi Rt$ is the area of cross-section with thickness $t \approx 2.8\,\text{nm}$ (Donhauser et al. 2010; Deriu et al. 2010), L_0 is the initial length and ΔL is the elongation in the axial direction. In Fig. 3b–d, the obtained results were presented against the PF number N, the helix-start number S and the skew angle θ, respectively, for the ten samples represented by N_S in the figures.

Here, Fig. 3b shows that for a given S, the Young's modulus E tends to increase slightly with rising N. In Fig. 3c, E also grows gradually with rising S. The increase of E due to growing S (Fig. 3c) is found to be more than 6 times greater than that caused by raising N (Fig. 3b). The relation between E and θ is not clearly observed in Fig. 3c, but θ is found to vary significantly with N (at a constant S) or S (at a constant N). This infers that the change of E in Fig. 3b and c results not only from the changes of S and N but also from the variation of the skew angle θ. Nevertheless, in Fig. 3d, the maximum change of $|\theta|$ (the absolute value) due to the variation of N (at a constant S) is $\sim$1.4° close to the corresponding angle change $\sim$1.7° caused by varying S (at a constant N). The influence of such minor skew angle changes should be trivial for the Young's modulus and thus can be ignored in the study of MTs.

Further, it is noted that, in Fig. 3, the Young's modulus E rises and falls around a mean value 0.83 GPa with the maximum value around 0.85 GPa and minimum value around 0.8 GPa. The deviation from the average value thus is less than 4 %. From these results, it follows that in general, the effect of the MT configuration characterized by N, S and

θ is insignificant for the Young's modulus of MTs. Thus, the average E of 0.83 GPa should be adequate in describing the E-related overall mechanical responses of MTs. In particular, it is found that the mean value of Young's modulus 0.83 GPa predicted based on the SM model for different MTs agrees well with 0.8 GPa obtained in an experiment (de Pablo et al. 2003) (the relative difference 4 %) and 0.9 GPa calculated for 13_3 MTs based on the AENM (Deriu et al. 2010) (the relative difference around 8 %). This comparison as well as those that will be shown later demonstrates the accuracy of the present SM model in characterizing the mechanical behaviour of MTs.

4.2 Configuration effect on shear modulus

In this section, we calculated the shear modulus of MTs based on the SM model. As shown in Fig. 3e, a torsional moment T_0 was applied to the free end of an MT to generate a torsional angle γ on the MT. The shear modulus G was then computed by $G = T_0 L_0/(\gamma J_0)$, where J_0 is the polar moment of inertia of the cross-sectional area. Considering MTs as hollow cylinders, we have $J_0 = (\pi/32)[(2R+t)^4 - (2R-t)^4]$. The obtained G was plotted vs. the PF number N, the helix-start number S and the skew angle θ in Fig. 3f–h, respectively. Here, $G = 47.1$ MPa was achieved for 13_3 MTs based on the SM model, which is more than two orders of magnitude lower than the Young's modulus 0.83 GPa. The result agrees well with 47 MPa (Sept and MacKintosh 2010) and 50 MPa (Deriu et al. 2010) reported in existing simulations. This shows another piece of evidence that the present SM model is reliable in studying the elastic properties of MTs.

As shown in Fig. 3f, G decreases almost linearly with increasing N when the helix-start number S is given. In the meantime, both Fig. 3g,f indicate that G also rises with growing S at the same PF number N. Very differently, in Fig. 3h, G does not seem to change monotonically with the skew angle θ. In fact, it is reasonable to believe that the θ-effect on the shear modulus G in the circumferential direction should be even smaller than that on the Young's modulus E in the axial direction and thus can be safely neglected in the mechanics of MTs. In other words, the shear modulus G of MTs is prominently determined by N and S. Furthermore, as seen from Fig. 3g, at $S = 3$, G decreases by 28 % when N increases from 12 to 15, while Fig. 3h indicates that at $N = 14$ G increases by 48 % as S grows from 2 to 4. Obviously, the relative change of G is much greater than that of E (<6.2 %) obtained in Sect. 4.1 for the same group of MTs. This comparison shows that the shear modulus G is much more sensitive to the change of configuration than is the Young's modulus E.

MTs can be imagined as hollow cylinders that are constructed by rolling up the two-dimensional PF sheets. Obviously, the mechanical properties of a perfectly flat PF sheet can only be tailored via the change in the helix angle ($\approx Sa/(N\delta x)$). Further changes of the properties would occur for the MTs primarily due to the curvature change achieved ($\approx 2\pi/(N\delta x)$) in the rolling up process. It is thus evident that PF number N and helix-start number S exert influence on the shear modulus (or Young's modulus) of MTs primarily by changing the two key factors, i.e., (1) the helix angle and (2) the curvature radius of the cylindrical PF nanotubes (i.e., MTs). Specifically, it is easy to see that a smaller N leads to a smaller radius of MTs, and a combination of smaller N and larger S results in a greater helix angle. Thus, the achieved N- and S-effects on the shear modulus (Fig. 3f,g) basically show that an MT of smaller radius and larger helix angle exhibits a higher shear modulus.

5 Bending stiffness of MTs

The bending stiffness is an important structure property of MTs which measures their ability to resist the bending deformation and the structural instability of MTs. In this section, the SM model was utilized to study the unique behaviours of the effective bending stiffness D of MTs. The free-fixed end conditions were considered for the sample MTs unless otherwise specified.

5.1 Length-dependence of the bending stiffness

First, let us examine the length-dependence of the effective bending stiffness D of MTs. In this study, 13_3 MTs were used as a typical example. As shown in Fig. 4, a transverse force F_2 was applied to the free end of the MT to generate the deflection f at the same place. The bending stiffness D of such a cantilever beam can then be evaluated by $D = F_2 L_0^3/(3f)$ (Gere 2003). The results were plotted (solid squares) in Fig. 4 against L_0, where D is found to increase considerably with rising L_0. The rate of change, however, decreases with growing L_0 and tends to be zero at large L_0, i.e., $L_0 > 400$ nm or the length-to-diameter ratio > 15. In other words, for such long MTs, the bending stiffness approaches a constant value independent of L_0. This behaviour of long MTs can be explained by the Euler beam theory, whereas for the length-dependent bending stiffness of short MTs, there exist two possible physical origins: (1) the effect of transverse shear deformation proposed for short classical beams in the Timoshenko beam (TB) theory (Gao and Lei 2009; Pampaloni et al. 2006) and (2) the nonlocal effect (Gao and Lei 2009; Shen 2010) expected for nanoscale beams like MTs and other nanotubes (Wang et al. 2008). In the nonlocal elasticity theory, the stress at a point in a body depends not only on the strain at that point but also on the rest of the points in the body. In this study, effort was invested to

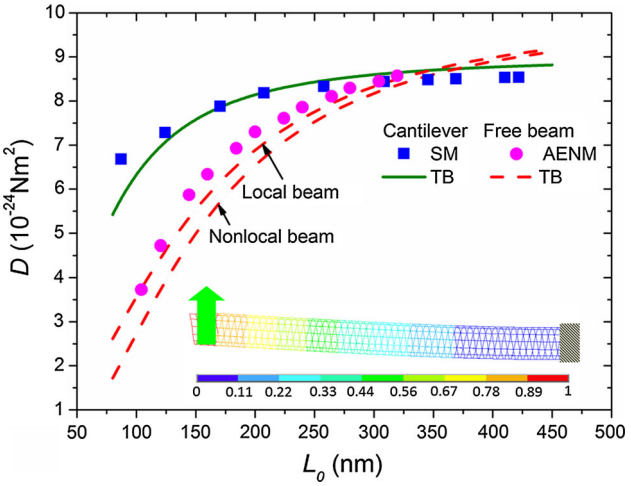

Fig. 4 The length (L_0)-dependent bending stiffness (D) calculated for 13_3 MTs as cantilever beams based on the SM model (the *solid blue squares*) and the classical TB model (the *solid green line*); and those obtained for free 13_3 MTs based on the AENM (the *solid pink circles*) (adopted from Deriu et al. (2010)), the classical TB model (the *upper red dashed line*) and the nonlocal TB model (the *lower red dashed line*). The *inset* shows the bending deformation of a 13_3 MT due to a transverse force acting on its free end

evaluate these two effects on the length-dependence of the bending stiffness D.

To achieve this goal, the classical TB model accounting for the shear deformation effect was used to calculate D of 13_3 MTs. The shear modulus G required in the calculation was obtained in Sec. 4 based on the SM model. The TB results (a solid line) were presented in Fig. 4 in comparison with those of the SM model (solid squares). It is seen that in general, a good agreement is achieved between the two models in predicting the bending stiffness D for MTs of different lengths. The results suggest that when L_0 falls in the range of (110, 400 nm), the obtained L_0-dependence of D can be ascribed primarily to the shear deformation effect. In spite of this, detectable discrepancy between the two models can still be observed at $L_0 < 110$ nm where the TB model predicts D lower than that given by the SM model. It seems that the classical TB model becomes less relevant to the mechanics of short MTs. This gap, however, cannot be closed by the nonlocal TB model, as the nonlocal effect would exert softening effect on the nanostructures. In other words, the difference between the nonlocal TB model and the SM model would be even greater than the discrepancy between the classical TB model and the SM model. Based on these results, we came to the conclusion that the shear deformation effect, rather than the nonlocal effect, should be mainly responsible for the length-dependence of D observed for MTs. This observation for MTs is in accordance with Wang et al.'s analysis for other cantilever micro/nanobeams (see the Supplementary Materials or Wang et al. 2008).

To further clarify this issue, we compared previously used AENM (Deriu et al. 2010) with the classical TB model and nonlocal TB model (Wang et al. 2008) in predicting the length-dependence of D for 13_3 MTs (Fig. 4). For the sake of comparison, the free-free end conditions (i.e., the two ends are free) used in (Deriu et al. 2010) were considered in the two TB models for the MTs and their bending stiffness D was extracted from the resonant frequency of free vibration (see details in the Supplementary Materials). It is seen from Fig. 4 that D obtained for the free MTs also grows with the rising length L_0. In particular, the classical TB model (upper dashed lines) fits the AENM (solid circles) very well, whereas substantial deviation from the AENM is observed for the nonlocal TB model (the lower dashed line). These results are qualitatively similar to those obtained for the MTs with the free-fixed end conditions. The results thus further confirm that the shear deformation is the main physical origin of the L_0-dependence of D. Moreover, in Fig. 4, the end constraints are found to play a significant role in determining D and its rate of change with the length, e.g., the free ends lead to lower bending stiffness D (at $L_0 < 400$ nm) but higher rate of change in D with the length. This issue deserves a detailed study in the near future. In Fig. 4, it is noted that the direct comparison between SM and AENM cannot be made due to the different boundary conditions considered. To overcome the difficulty, the classical TB model is used as a reference and found to agree well with the two discreet models when the same boundary conditions are considered for the sample MTs. This result suggests that the SM model and AENM (Deriu et al. 2010) are in accordance with each other.

5.2 Effect of MT configuration on the bending stiffness

In this section, the attention was paid to the influence of the MT configuration on the bending stiffness. According to Fig. 4, the transverse shear effect on D becomes negligible for long MTs of $L_0 > 400$ nm or the length-to-diameter ratio > 15. In this case, D is a constant independent of the length. Thus, to avoid the influence of the length and focus our attention on the effect of MT configuration, we considered the MTs of $L_0 > 400$ nm. The bending stiffness D of the MTs was then calculated as a function of the skew angle θ and the helix-start number S in Fig. 5a,b. First, Fig. 5a shows the trivial role of θ in determining D of the MTs. Similarly, it is found in Fig. 5b that the helix-start number S cannot substantially change D either. Such small effect of θ and S on D given by the SM model is consistent with that reported in existing MD simulations (Molodtsov et al. 2005), elastic sheet modelling (Janosi et al. 1998) and finite element analysis (Donhauser et al. 2010). On the other hand, strong N-dependence is achieved in Fig. 5 for D of MTs, where D increases with rising N by up to 50 %. N therefore is

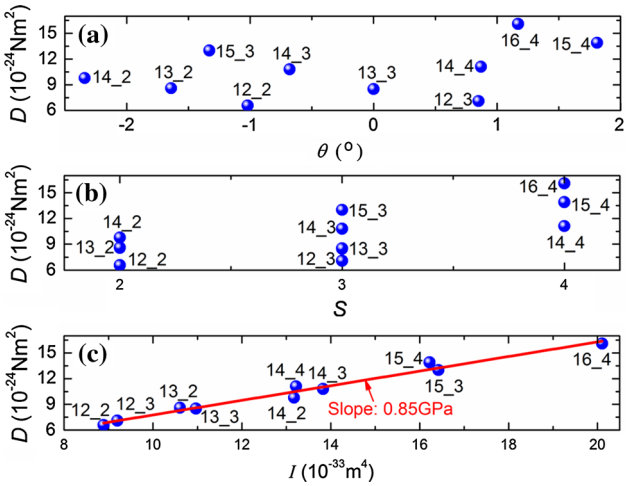

Fig. 5 The bending stiffness (D) of MTs as a function of (**a**) the PF skew angle θ, (**b**) the helix-start number S and (**c**) the moment of inertia I

identified as the major factor responsible for the D-variation shown in Fig. 5. The N-dependence may be understood based on the fact that a greater N leads to a larger diameter and accordingly, a higher moment of inertia I of the MTs. This would finally lead to the growth of D that increases with rising I. To confirm this theory, the D–I relation was plotted for the MTs in Fig. 5c, where in computing I we took 2.8 nm as the equivalent thickness of MTs (Donhauser et al. 2010; Deriu et al. 2010). As expected, in Fig. 5c, D is found to be proportional to I that grows monotonically with increasing N. On the other hand, at fixed N, S only changes I and D of the MTs slightly. These results validate the above theory of the N-dependence of D and offer a theoretical explanation for the similar experimental observation reported in Valdman et al. (2012) and Hawkins et al. (2012).

According to the Euler beam theory ($D = E \cdot I$), the slope of the D–I curve in Fig. 5c yields the average Young's modulus of MTs. The value obtained in Fig. 5c is 0.85 GPa very close to the average value 0.83 GPa (Fig. 3b) measured in the tensile tests. Considering that N of existing MTs varies widely from 8 to 17, the bending stiffness D ($= E \cdot I$) of existing MTs would fall in the range of [2.2×10^{-24}N m^2, 20.2×10^{-24}N m^2], which is in perfect agreement with [1.9×10^{-24}N m^2, 21.5×10^{-24}N m^2] reported in previous experiments (Felgner et al. 1996; Gittes et al. 1993; Kawaguchi and Yamaguchi 2010).

5.3 Persistence length

In this section, the bending stiffness D obtained for the MTs was used to calculate the persistence length of MTs, which describes MTs' resistance to the thermal forces. The persistence length can be defined as the length of the MTs, over which thermal bending becomes appreciable, or the length of the MTs over which tangent–tangent correlation is destroyed by thermal fluctuations. When the length of MTs is shorter than the persistence length, the MTs behave like a flexible elastic rod where the correlation remains between orientational orders. On the other hand, as the length exceeds the persistence length, the orientational correlation of MTs is lost and their structural dynamic properties can only be described statistically. In the theory, an effective persistence length L_p is determined by (Pampaloni et al. 2006)

$$L_p = \frac{D}{kT} \cdot \left(1 + \frac{3D}{K_s G A_0 L_0^2}\right)^{-1} \tag{9}$$

where k and T are the Boltzmann's constant and the temperature; K_s is a geometrical correction factor.

Previously, to estimate L_p based on Eq. 9, 13_3 MTs were usually selected as a typical example which possesses a constant bending stiffness D. The persistence length reported for MTs is thus of a constant value. This, however, is in contradiction with the large scattering of the experimental data represented by solid circles in Fig. 6 (Brangwynne et al. 2007; Valdman et al. 2012; Van den Heuvel et al. 2008; Janson and Dogterom 2004). To understand the broad distribution of the persistence length, we have incorporated the N-dependence of D achieved in the Sec. 5.2 into Eq. 9. The persistence length then was calculated in Fig. 6 based on the Eq. 9 (lines) for the MTs with N growing from 8 to 17 and L_0 increasing from 1 μm to 70 μm. In this calculation, the values of parameters chosen for MTs were as follows: $k = 8.62 \times 10^{-5}$eV/K, $T = 290$ K and $K_s = 0.72$ for the MT (Pampaloni et al. 2006; Deriu et al. 2010), a hollow cylindrical structure with circular cross-section.

It is noted that the MTs studied in experiments usually possess the contour length L_0 much greater than 400 nm. As stated in Sects. 5.1 and 5.2, the bending stiffness D of such long MTs is primarily determined by the PF number N but independent of the length L_0. Thus, in Fig. 6, a greater N will lead to a larger D and accordingly, the growth of the persistence length. For example, when N is raised from 8 to 17, the persistence length would grow from 0.5 to 5.1 mm by a factor of 10 due to the increment of D. On the other hand, in Fig. 6, the contour length-dependence is not observed for the persistence length predicted by Eq. 9 as $3D/(K_s G A L_0^2) << 1$ when $L_0 \geq 1$ μm. The negligible length-dependence of persistence length has been confirmed in most existing experiments (e.g., Gittes et al. 1993; Venier et al. 1994; Valdman et al. 2012; Hawkins et al. 2012, 2013) except Pampaloni et al. (2006) and Kawaguchi and Yamaguchi (2010). Thus, N can be identified as a major geometric parameter that determines the persistence length of MTs. In particular, this N-dependence of L_p can partially explain the large scattering of the persistence length achieved in existing experiments.

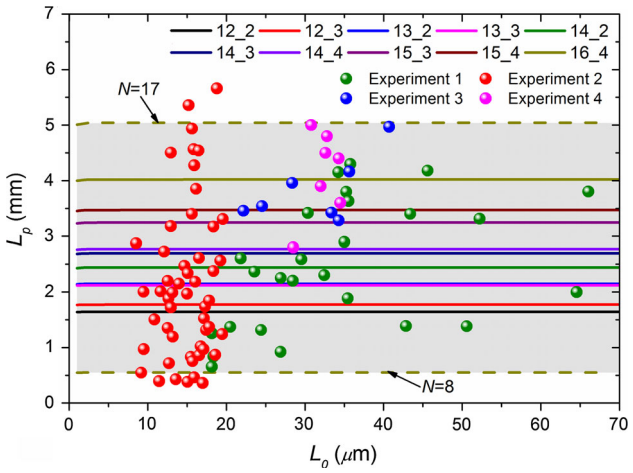

Fig. 6 The persistence length (L_p) of different types of MTs as a function of their length (L_0), calculated by using Eq. (9) with N-dependent D (*lines*) and measured in the experiments (the *solid circles*) (experiments 1 to 4 are, respectively, adopted from Brangwynne et al. 2007; Valdman et al. 2012; Van den Heuvel et al. 2008 and Janson and Dogterom 2004)

Nevertheless, it is also noticed that in most experiments, N normally ranges between 12 and 15 (see Table 1 or Chretien and Wade 1991 or Hawkins et al. 2012) rather than 8–17. As shown in Fig. 6, this leads to the variation of the theoretically predicted L_p from 1.6 to 3.5 mm, which is smaller than the scattering range of the persistence length (0.4–5.6 mm) achieved in the experiments (Fig. 6). This comparison suggests that in addition to the PF number N, other external and internal factors (e.g., temperature, experimental conditions, etc.) may also have a role in distributing the persistence length of MTs measured experimentally.

6 Conclusions

In the present study, an SM model is developed to account for the effect of the molecular structures of MTs on their mechanical properties. The technique proven to be accurate in its applications can improve the efficiency and expand the scope of the research as compared with formidable MD simulations and difficult nanoscale experiments. The development of the novel characterizing technique is thus a major contribution of the present work to the research on biomechanics.

Based on the SM model, the first comprehensive study is conducted for the configuration effect on the Young's modulus, shear modulus, bending stiffness and persistence length of MTs. The systematic research on this issue is of practical interest but still remains challenging for existing simulation and experimental techniques. It is found that the Young's modulus has a nearly constant value around 0.83 GPa independent of MT configurations. The shear modulus is two orders of magnitude lower and can increase by up to 48 % as the PF number decreases or the helix-start number increases. Accordingly, a thinner MT of a lager helix angle exhibits a higher shear modulus. In addition, the bending stiffness D increases considerably with growing PF number N and show substantial length-dependence for relatively short MTs (e.g., the length <400 nm). In particular, the D–N relation leads to the strong N-dependence of the persistence length, which is partially responsible for the wide distribution of the persistence length obtained in existing experiments.

Moreover, it should be pointed out that, other than the study of individual MTs, the SM model can also be employed to study the MTs grafted with other biomolecules and has potential to be further extended to the study of actin and intermediate filaments (Chu and Voth 2005; Chandran and Mofrad 2009), the other two structural elements in eukaryotic cells. The major challenge here is to obtain the parameters describing the interaction between the different proteins or biomolecules.

Acknowledgments JZ acknowledges the support from the China Scholarship Council (CSC).

References

Alberts B, Johnson A, Lewis J, Raff M, Roberts K, Walter P (2002) Molecular biology of the cell, 4th edn. Garland Science, New York

Brangwynne CP, Koenderink GH, Barry E, Dogic Z, MacKintosh FC, Weitz DA (2007) Bending dynamics of fluctuating biopolymers probed by automated high-resolution filament tracking. Biophys J 93:346–359

Chandran PL, Mofrad MRK (2009) Rods-on-string idealization captures semiflexible filament dynamics. Phys Rev E 79:011906

Chretien D, Wade RH (1991) New data on the microtubule surface lattice. Biol Cell 71:161–174

Chretien D, Fuller SD (2000) Microtubules switch occasionally into unfavorable configurations during elongation. J Mol Biol 298:663–676

Chu JW, Voth GA (2005) Allostery of actin filaments: molecular dynamics simulations and coarse-grained analysis. Proc Natl Acad Sci USA 102:13111–13116

de Pablo PJ, Schaap IAT, MacKintosh FC, Schmidt CF (2003) Deformation and collapse of microtubules on the nanometer scale. Phys Rev Lett 91:098101

Deriu MA, Enemark S, Soncini M, Montevecchi FM, Redaelli A (2007) Tubulin: from atomistic structure to supramolecular mechanical properties. J Mater Sci 42:8864–8872

Deriu MA, Soncini M, Orsi M, Patel M, Essex JW, Montevecchi FM, Redaelli A (2010) Anisotropic elastic network modeling of entire microtubules. Biophys J 99:2190–2199

Donhauser ZJ, Jobs WB, Binka EC (2010) Mechanics of microtubules: effects of protofilament orientation. Biophys J 99:1668–1675

Enemark S, Deriu MA, Soncini M, Redaelli A (2008) Mechanical model of the tubulin dimer based on molecular dynamics simulations. J Biomech Eng 130:041008

Felgner H, Frank R, Schliwa M (1996) Flexural rigidity of microtubules measured with the use of optical tweezers. J Cell Sci 109:509–516

Gao YW, Lei FM (2009) Small scale effects on the mechanical behaviors of protein microtubules based on the nonlocal elasticity theory. Biochem Biophys Res Commun 387:467–471

Gebremichael Y, Chu JW, Voth GA (2008) Intrinsic bending and structural rearrangement of tubulin dimer: molecular dynamics simulations and coarse-grained analysis. Biophys J 95:2487–2499

Gere JM (2003) Mechanics of Materials, 5th edn. Brooks/Cole, Pacific Grove California

Gittes F, Mickey B, Nettleton J, Howard J (1993) Flexural rigidity of microtubules and actin filaments measured from thermal fluctuations in shape. J Cell Biol 120:923–934

Hawkins T, Mirigian M, Yasar MS, Ross JL (2010) Mechanics of microtubules. J Biomech 43:23–30

Hawkins TL, Mirigian M, Li J, Yasar MS, Sackett DL, Sept D, Ross JL (2012) Perturbations in microtubule mechanics from tubulin preparation. Cell Mol Bioeng 5:227–238

Hawkins TL, Sept D, Mogessie B, Straube A, Ross JL (2013) Mechanical properties of doubly stabilized microtubule filaments. Biophys J 104:1517–1528

Howard J (2001) Mechanics of motor proteins and the cytoskeleton. Sunderland, MA

Howard J, Hyman AA (2003) Dynamics and mechanics of the microtubule plus end. Nature 422:753–758

Hunyadi V, Chretien D, Janosi IM (2005) Mechanical stress induced mechanism of microtubule catastrophes. J Mol Biol 348:927–938

Hunyadi V, Chretien D, Flyvbjerg H, Janosi IM (2007) Why is the microtubule lattice helical? Biol Cell 99:117–128

Janosi IM, Chretien D, Flyvbjerg H (1998) Modeling elastic properties of microtubule tips and walls. Eur Biophys J 27:501–513

Janson ME, Dogterom M (2004) A bending mode analysis for growing microtubules: evidence for a velocity-dependent rigidity. Biophys J 87:2723–2736

Ji XY, Feng XQ (2011a) Coarse-grained mechanochemical model for simulating the dynamic behavior of microtubules. Phys Rev E 84:031933

Ji XY, Feng XQ (2011b) Mechanochemical modeling of dynamic microtubule growth involving sheet-to-tube transition. PLoS ONE 6:e29049

Kasas S, Kis A, Riederer BM, Forro L, Dietler G, Catsicas S (2004) Mechanical properties of microtubules explored using the finite elements method. Chem Phys Chem 5:252–257

Kawaguchi K, Yamaguchi A (2010) Temperature dependence rigidity of non-taxol stabilized single microtubules. Biochem Biophys Res Commun 402:66–69

Kikumoto M, Kurachi M, Tosa V, Tashiro H (2006) Flexural rigidity of individual microtubules measured by a buckling force with optical traps. Biophys J 90:1687–1696

Li CY, Chou TW (2003) A structural mechanics approach for the analysis of carbon nanotubes. Int J Solids Struct 40:2487–2499

Li T (2008) Mechanics model of microtubule buckling in living cells. J Biomech 41:1722–1729

Mehrbod M, Mofrad MRK (2011) On the significance of microtubule flexural behavior in cytoskeletal mechanics. PLoS ONE 6:e25627

Mitra A, Sept D (2008) Taxol allosterically alters the dynamics of the tubulin dimer and increases the flexibility of microtubules. Biophys J 95:3252–3258

Mizushima-Sugano J, Maeda T, Miki-Noumura T (1983) Flexural rigidity of singlet microtubules estimated from statistical analysis of their contour lengths and end-to-end distances. Biochim Biophys Acta 755:257–262

Molodtsov MI, Ermakova EA, Shnol EE, Grishchuk EL, McIntosh JR, Ataullakhanov FI (2005) A molecular-mechanical model of the microtubule. Biophys J 88:3167–3179

Pampaloni F, Florin EL (2008) Microtubule architecture: inspiration for novel carbon nanotube-based biomimetic materials. Trends Biotechnol 26:302–310

Pampaloni F, Lattanzi G, Jonas A, Surrey T, Frey E, Florin EL (2006) Thermal fluctuations of grafted microtubules provide evidence of a length-dependent persistence length. Proc Natl Acad Sci USA 103:10248–10253

Schaap IAT, Hoffmann B, Carrasco C, Merkel R, Schmidt CF (2007) Tau protein binding forms a 1 nm thick layer along protofilaments without affecting the radial elasticity of microtubules. J Struct Biol 158:282–292

Sept D, MacKintosh FC (2010) Microtubule elasticity: connecting all-atom simulations with continuum mechanics. Phys Rev Lett 104:018101

Shen HS (2010) Nonlocal shear deformable shell model for postbuckling of axially compressed microtubules embedded in an elastic medium. Biomech Model Mechanobiol 9:345–357

Sirenko YM, Stroscio MA, Kim KM (1996) Elastic vibrations of microtubules in a fluid. Phys Rev E 53:1003–1010

Valdman D, Atzberger PJ, Yu D, Kuei S, Valentine MT (2012) Spectral analysis methods for the robust measurement of the flexural rigidity of biopolymers. Biophys J 102:1144–1153

VanBuren V, Cassimeris L, Odde DJ (2005) Mechanochemical model of microtubule structure and self-assembly kinetics. Biophys J 89:2911–2926

Van Buren V, Odde DJ, Cassimeris L (2002) Estimates of lateral and longitudinal bond energies within the microtubule lattice. Proc Natl Acad Sci USA 99:6035–6040

Van den Heuvel MGL, de Graaff MP, Dekker C (2008) Microtubule curvatures under perpendicular electric forces reveal a low persistence length. Proc Natl Acad Sci USA 105:7941–7946

Venier P, Maggs AC, Carlier MF, Pantaloni D (1994) Analysis of microtubule rigidity using hydrodynamic flow and thermal fluctuations. J Biol Chem 269:13353–13360

Wang CM, Kitipornchai S, Lim CW, Eisenberger M (2008) Beam bending solutions based on nonlocal Timoshenko beam theory. J Eng Mech 134:475–481

Wang CY, Ru CQ, Mioduchowski A (2006a) Vibration of microtubules as orthotropic elastic shells. Physica E 35:48–56

Wang CY, Ru CQ, Mioduchowski A (2006b) Orthotropic elastic shell model for buckling of microtubules. Phys Rev E 74:052901

Wang CY, Li CF, Adhikari S (2009) Dynamic behaviors of microtubules in cytosol. J Biomech 42:1270–1274

Wang CY, Zhang LC (2008) Circumferential vibration of microtubules with long axial wavelength. J Biomech 41:1892–1896

Weaver W Jr, Gere JM (1990) Matrix analysis of framed structures, 3rd edn. Van Nostrand Reinhold, New York

Wu ZH, Nogales E, Xing JH (2012) Comparative studies of microtubule mechanics with two competing models suggest functional roles of alternative tubulin lateral interactions. Biophys J 102:2687–2696

Zhang J, Wang CY, Adhikari S (2013) Molecular structure-dependent deformations in boron nitride nanostructures subject to an electrical field. J Phys D: Appl Phys 46:235303